Int J Adv Manuf Technol (2010) 50:961–977
DOI 10.1007/s00170-010-2574-x

ORIGINAL ARTICLE

The effect of tool edge radius on the chip formation behavior of tool-based micromachining

Keng Soon Woon · Mustafizur Rahman

Received: 18 May 2009 / Accepted: 8 February 2010 / Published online: 17 March 2010

Abstract Chip formation behavior of micromachining is governed by the tool edge radius effect as reflected by the characteristic changes in plastic deformation at varying combinations of tool edge radius, r, and undeformed chip thickness, a. At high a/r above unity, concentrated plastic deformation takes place at the primary and secondary deformation zones akin to conventional macromachining. Decreasing a/r below unity promotes localized deformation ahead of the tool edge radius, with the expansion in fraction of the primary deformation zone and the simultaneous shrinkage in fraction of the secondary deformation zone following the reductions in total tool–chip contact length. Further decrease of a/r below a critical threshold brings forth a total suppression of secondary deformation zone and resulted in an ultimate localization of plastic deformation ahead of the tool edge radius. This is perceived as a transition in chip formation mechanism from concentrated shearing to a thrust-oriented behavior.

Keywords Tool edge radius effect · Micromachining · Plastic deformation · Finite element method

K. S. Woon · M. Rahman
Department of Mechanical Engineering,
National University of Singapore,
10 Kent Ridge Crescent,
119260 Singapore, Singapore

K. S. Woon
Singapore Institute of Manufacturing Technology,
Machining Technology Group,
71 Nanyang Drive,
638075 Singapore, Singapore
e-mail: mpemusta@nus.edu.sg

1 Introduction

Tool edge radius effect in micromachining arises when undeformed chip thickness, a, is comparable to the size of tool edge radius, r, at fine magnitudes of material removal. Observations based on experimental and modeling studies indicate the significance of such tool edge radius effect on the behavior of chip formation.

Such an effect was first identified by Masuko [1] and subsequently validated by Albrecht [2] in a separate experimental study. Through the machining of aluminum alloy and carbon steel, Masuko [1] discovered that the cutting force consisted of the chip formation component and the indentation component which arose by the tool edge radius. Extrapolation of cutting force at $a=0$ μm suggested the magnitude of the indenting action. Subsequently, Finnie [3] claimed that the indentation effect on material removal was not significant for a of several millimeters, but conceded that it could be significant in grinding. These findings have thus pointed out the importance of such effect in fine-scale machining.

In addition, Bitans and Brown [4] reported that plastic deformation was governed by tool edge radius, r, and rake angle, γ, where thicker plastic shear zone was induced by larger r and γ. Nakayama and Tamura [5] encountered a nonlinear increase in specific cutting and thrust forces at reducing cutting depths in micron scale where these machining phenomena were attributed to the tool edge radius effect through the extension of shear zone. These were recognized by Abdelmoneim and Scrutton [6] only under a unique condition of $a \leq r\,(1 + \sin \gamma_{\text{tool}})$. On the other hand, Basuray et al. [7] claimed non-uniform material displacement at a critical a larger than r. Later, Komanduri et al. [8] confirmed the significance of tool edge radius

effect in nanometric cutting with molecular dynamics simulation at fine undeformed chip thicknesses.

Through orthogonal fly cutting, Moriwaki and Okuda [9] reported that the dominance of plastic deformation would increase cutting resistance rather than sheared cutting. According to Ikawa [10], a third deformation zone between the machined surface and clearance face was driven by elastic recovery at decreasing a/r due to the tool edge radius effect. Lucca et al. [11] also pointed out that elastic recovery would cause material plowing and flank face rubbing that increased the specific cutting energy. These experimental observations agree well with the finite element analyses reported by Moriwaki et al. [12]. At $a/r < 1$, Lucca et al. [13] encountered that the resultant force was directed toward the thrust direction, which might influence the behavior of chip formation. Under such a condition, Inamura et al. [14] determined that chip formation could be due to yield stress rather than shearing through atomic-based simulations as concentrated shear stress in the primary deformation zone (PDZ) was absent. With this observation, Inamura et al. [15] claimed that the deformation mechanism was a kind of buckling deformation when the area was highly compressed.

More recently, various experimental and computational modeling studies revealed great influences of the tool edge radius effect in ductile-mode machining of brittle materials. Through ultra-precision cutting of single crystal silicon, Fang and Zhang [16] reported that ductile-mode machining could take place at an effective negative rake angle through the control of varying r and a. Liu et al. [17] found that the critical a for ductile–brittle transition in chip formation increases linearly with the r used, while the values of the critical a are close to the values of r. Moreover, Arefin et al. [18] reported that r has to be greater than a, but the size of r must not exceed an upper bound value of approximately 800 nm to yield a crack-free machined surface of single-crystal silicon. This phenomenon is related to the distributions of tensile stress as elucidated by Li et al. [19] through molecular dynamics simulation.

Careful examination of these prominent studies in the past discloses that the subject of interest was previously approached from limited angles. In particular, the interrelationship between chip formation behavior and tool–chip tribological characteristic has never been evaluated to a satisfactory extent. Although four regions of contact stress on tool rake and clearance faces, along the tool edge radius, and across the material deformation zone were reported by Kim and Kim [20], the concept was not expanded for a wider, practical range of a/r.

The importance of this aspect is reflected by the changing contact behavior that affects the loading conditions along the contact interfaces and thus the behavior of chip formation. For instance, the establishment of secondary deformation zone (SDZ) is governed by the development of tool–chip contact length on the rake face which influences the intensity of plastic deformation during the process. This is due to the transmission of major external loading from the cutting tool along the contact interfaces. Such a phenomenon will not be encountered if perfect edge sharpness is assumed because the responses of tribological and deformation activities would be linear, being solely governed by the magnitudes of a and γ.

Thus, this study was intended to elucidate the tool edge radius effect on the chip formation behavior through a concurrent evaluation approach on both tribological and plastic deformation characteristics. It was performed with an advanced finite element (FE) modeling technique based on the arbitrary Lagrangian–Eulerian (ALE) method in which the tool edge radius effect was quantified as the relative tool sharpness, a/r. It should be noted that the experimental method is limited in fundamental study of this sort due to the fine magnitudes of material removal involved, which increase the difficulty and cost in extracting fundamental data from such fine deformation zones. With the availability of advanced computing technology, the ALE-FE method appears to be a more viable and cost-effective solution.

2 ALE-FE micromachining analysis

The effect of tool edge radius on chip formation behavior is studied in its orthogonal configuration under plane strain and explicit dynamic conditions. Material removal through micromachining is achieved with free nodal motion to avoid the incorporations of unrealistic chip separation criteria. Mesh quality during severe deformation is maintained through independent nodal motion from the material point. The building blocks of the model are illustrated in Fig. 1.

2.1 Model configuration and boundary conditions

The model consisted of the steel workpiece and the WC-Co cutter. Medium carbon steel (AISI 1045) is chosen as the workpiece due to its superiority in machinability and strength suitable for miniaturized components. The workpiece is treated as a rectangular block (160×50 μm) in the model, and the cutter is modeled with varying tool rake angle, γ of −10°, 0°, and 10°, uniform clearance angle, α of 6°, and tool edge radius, r of 10 μm, based on actual geometries. The length of the cutting edge is approximately 16 μm, close to that of the cutters for experimental validation (Section 3). The workpiece and cutter are meshed with four-node bilinear (1×0.5 μm) and three-node linear (1.5 μm) coupled temperature-displacement

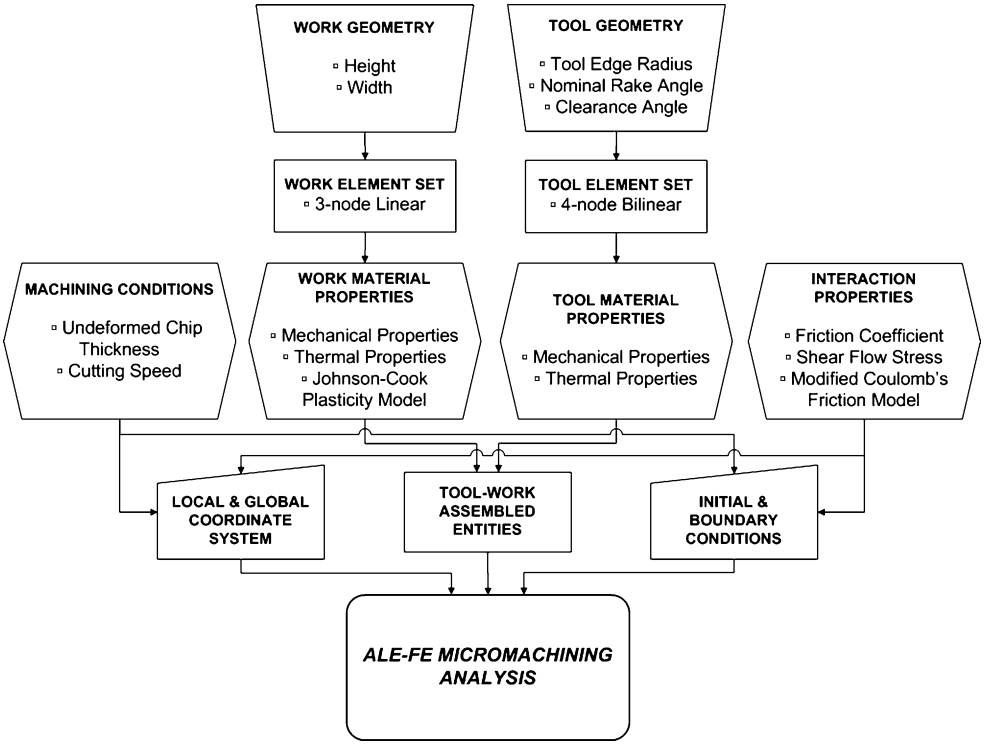

Fig. 1 Illustration of the building elements and work flow of the arbitrary Lagrangian–Eulerian finite element model for tool-based micromachining

elements, respectively. Configuration of the model is shown in Fig. 2.

To initiate material removal, workpiece is fed horizontally toward the rigid cutting tool at various cutting speed, V. The boundary conditions are (1) oy, $v_x=V$; (2) ox, $v_y=0$; (3) st, $u_y=0$; (4) tu, $u_x=0$; and (5) yz is unrestricted, where v_x, u_x, v_y, and u_y are nodal velocities and displacements in the x and y directions, respectively. Line yz is treated as the chip-free boundary so that chip shape is not fixed artificially. The range of undeformed chip thickness, a, attempted range from 2 to 20 μm, which yields a/r from 0.2 to 2.0 with r of 10 μm. Table 1 summarizes material properties, tribology, and operating conditions.

2.2 Description of motion

The ALE-FE framework consisted of three computational domains which comprise reference coordinates χ, material coordinates X, and spatial coordinates x, respectively [22], as shown in Fig. 3. The domains are connected through one-to-one transformation φ, Φ, and Ψ as interrelated by Eq. 1:

$$\varphi = \Phi \circ \Psi^{-1}. \tag{1}$$

The motion of material particles is connected to the spatial domain through φ as given in Eq. 2:

$$\varphi : R_X \times [t_0, t_{final}[\rightarrow R_x \times [t_0, t_{final}[(\chi, t) \mapsto \varphi(\chi, t) = (x, t) \tag{2}$$

and its gradient is represented by its matrix form in Eq. 3:

$$\frac{\partial \varphi}{\partial (X,t)} = \begin{pmatrix} \frac{\partial x}{\partial X} & v \\ \mathbf{0}^T & 1 \end{pmatrix} \tag{3}$$

where $\mathbf{0}^T$ is a null row vector, and the material velocity is expressed in Eq. 4:

$$v(X,t) = \left.\frac{\partial x}{\partial t}\right|_x. \tag{4}$$

Besides, the motion of the nodal points in the spatial configurations is determined by Eq. 5 through the mapping of the referential domain into the spatial domain:

$$\Phi : R_\chi \times [t_0, t_{final}[\rightarrow R_x \times [t_0, t_{final}[(\chi, t) \mapsto \Phi(\chi, t) = (x, t). \tag{5}$$

The gradient form is shown in Eq. 6:

$$\frac{\partial \Phi}{\partial (\chi,t)} = \begin{pmatrix} \frac{\partial x}{\partial \chi} & \hat{v} \\ \mathbf{0}^T & 1 \end{pmatrix} \tag{6}$$

while the nodal velocity is written as Eq. 7:

$$\hat{v}(\chi,t) = \left.\frac{\partial x}{\partial t}\right|_\chi. \tag{7}$$

The reference coordinates are used to establish nodal points in the domain. Material motion in the referential

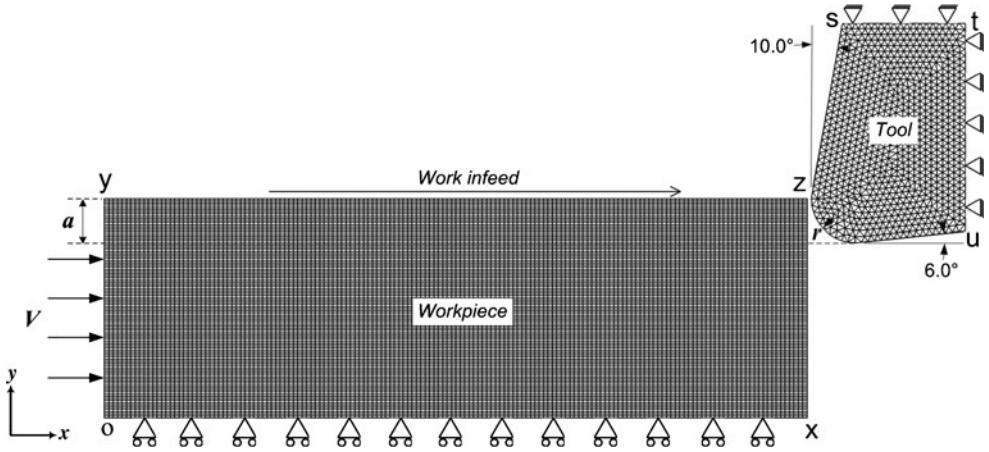

Fig. 2 Configuration of computationally meshed cutter–workpiece entities with predefined boundary conditions in the ALE domain. $\gamma = +10°, 0°, -10°$; $\alpha = 6°$; and $r = 10$ μm (example is shown for $\gamma = +10°$)

configuration is reflected from the mapping of which Ψ is usually represented in its inverse manner given as Eq. 8:

$$\boldsymbol{\Psi}^{-1} : R_X \times \left[t_0, t_{final}\right[\rightarrow R_\chi \times \left[t_0, t_{final}\right[(X,t) \mapsto \boldsymbol{\Psi}^{-1}(X,t) = (\chi,t) \tag{8}$$

Table 1 Operating conditions, tribological parameters, tool and workpiece properties

Orthogonal cutting conditions	
Cutting speed (m/min)	100, 250, 500
Tool rake angle (deg)	+10, 0, −10
Tool clearance angle (deg)	+6
Coefficient of friction (kinetic)	0.45
Frictional shear strength (MPa)	319.3
Tool edge radius, r (μm)	10
Undeformed chip thickness, a (μm)	2, 4, 6…20
Relative tool sharpness, a/r	0.2, 0.4, 0.6…2.0
AISI 1045 workpiece properties	
Thermal expansion (μm/m°C)	11
Density (g/cm^3)	7.8
Poisson ratio	0.3
Specific heat (J kg^{-1}°C^{-1})	432.6
Thermal conductivity (W/m°C)	47.7
Young's modulus (GPa)	200
AISI 1045J-C constants [21]	
A (MPa)	553.1
B (MPa)	600.8
n	0.234
C	0.013
m	1.000
WC-Co cutting tool properties	
Thermal expansion (μm/m°C)	4.7
Density (g/cm^3)	15
Poisson ratio	0.2
Specific heat (J kg^{-1}°C^{-1})	203
Thermal conductivity (W/m°C)	46
Young's modulus (GPa)	800

and the gradient is represented by Eq. 9:

$$\frac{\partial \Psi^{-1}}{\partial (X,t)} = \begin{pmatrix} \frac{\partial \chi}{\partial X} & w \\ 0^T & 1 \end{pmatrix} \tag{9}$$

where the velocity is calculated by Eq. 10:

$$w = \left.\frac{\partial \chi}{\partial t}\right|_X \tag{10}$$

The velocities given in Eqs. 4, 7, and 10 could be related by differentiating Eq. 2, which yields Eqs. 11 and 12:

$$v = \hat{v} + \frac{\partial x}{\partial \chi} \times w \tag{11}$$

$$\mathbf{D} = \begin{pmatrix} \frac{\partial x}{\partial \chi} & \hat{v} \\ \mathbf{0}^T & 1 \end{pmatrix} \begin{pmatrix} \frac{\partial \chi}{\partial X} & w \\ 0^T & 1 \end{pmatrix} \tag{12}$$

where **D** is the ALE gradient of deformation.

Conservations of mass, momentum, and energy are constantly observed.

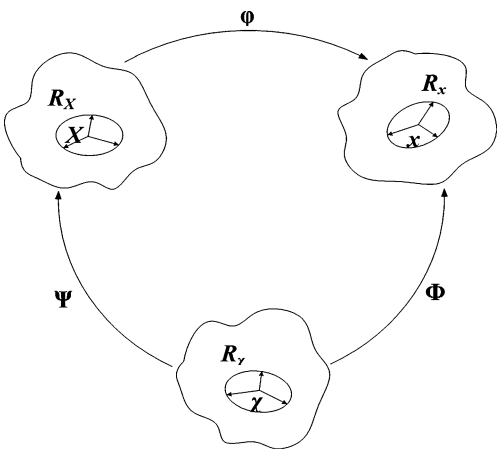

Fig. 3 Referential domain, $R\chi$, material domain, RX, and spatial domain, Rx, in the ALE framework associated with reference coordinates, $\boldsymbol{\chi}$, material particles, $\boldsymbol{X}$, and spatial points, $\boldsymbol{x}$, respectively. Domains are connected through single mapping φ, Φ, and Ψ. [18]

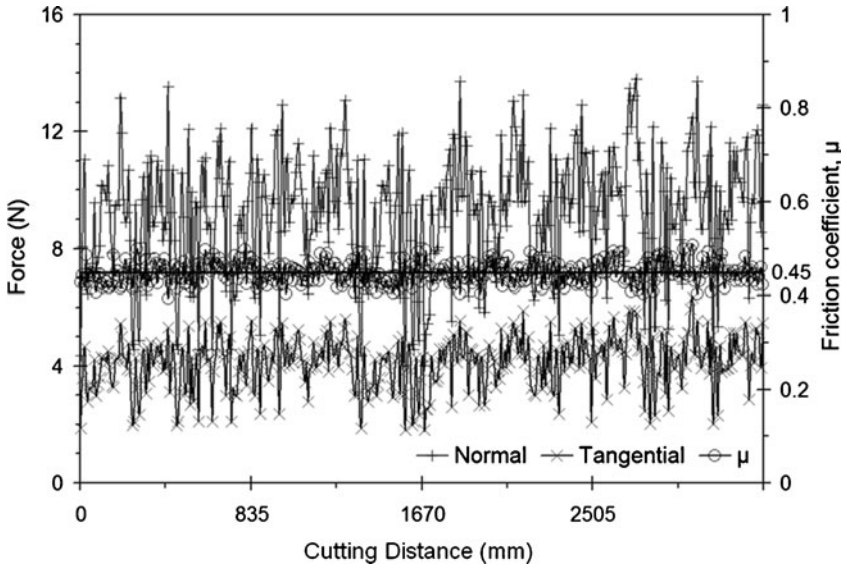

Fig. 4 Mean friction coefficient, μ_{mean}, of tool–workpiece under dry condition

2.3 States of deformation

During external loading, the most deformed material yields plastically, while the rest responds elastically, usually a significantly smaller portion. The nature of such deformation is characterized with rigid body rotation and principal elongation according to the polar decomposition theorem [23] as in Eq. 13:

$$\mathbf{D} = \mathbf{L} \times \mathbf{R} \tag{13}$$

where **L** and **R** are the elongation and rotation tensors. The elastic deformation component could thus be written as Eq. 14:

$$\mathbf{D}_t^{\text{el}} = \mathbf{L}_t^{\text{el}} \times \mathbf{R}_t^{\text{el}} \tag{14}$$

The behavior of deformation in metallic materials with sufficient ductility is of elastic–plastic nature. Total deformation gradient consists of the plastic and elastic components as represented by Eq. 15:

$$\mathbf{D} = \mathbf{D}_t^{\text{pl}} \times \mathbf{D}_t^{\text{el}} \tag{15}$$

while the gradients of elastic and plastic deformation velocities are derived as Eqs. 16 and 17, respectively:

$$\mathbf{S}^{el} = \dot{\mathbf{D}}^{el} \times \left(\mathbf{D}^{el}\right)^{-1} \tag{16}$$

$$\mathbf{S}^{pl} = \dot{\mathbf{D}}^{pl} \times \left(\mathbf{D}^{pl}\right)^{-1} \tag{17}$$

Thus, the total gradient of deformation velocity is expressed as Eq. 18:

$$\mathbf{S} = \dot{\mathbf{D}} \times \mathbf{D}^{-1} = \dot{\mathbf{D}}^{el} \times \left(\mathbf{D}^{el}\right)^{-1} + \mathbf{D}^{el} \times \dot{\mathbf{D}}^{el} \times \left(\mathbf{D}^{pl}\right)^{-1} \times \left(\dot{\mathbf{D}}^{\text{el}}\right)^{-1} \tag{18}$$

2.4 Plastic behavior

Plastic deformation of steel workpiece is modeled with the Johnson–Cook (J-C) plasticity model [24] in the form of equivalent stress as given in Eq. 19:

$$\sigma = \left(A + B\varepsilon_{\text{eq}}^{n}\right)\left[1 + C\ln\left(\frac{\dot{\varepsilon}_{eq}}{\dot{\varepsilon}_0}\right)\right]\left[1 - \left(\frac{T - T_r}{T_m - T_r}\right)^{m}\right] \tag{19}$$

where A, B, C, m, and n are strength coefficients referring to yield strength, hardening modulus, strain rate sensitivity,

Fig. 5 Ultra-precision machine tool for micromachining experiments

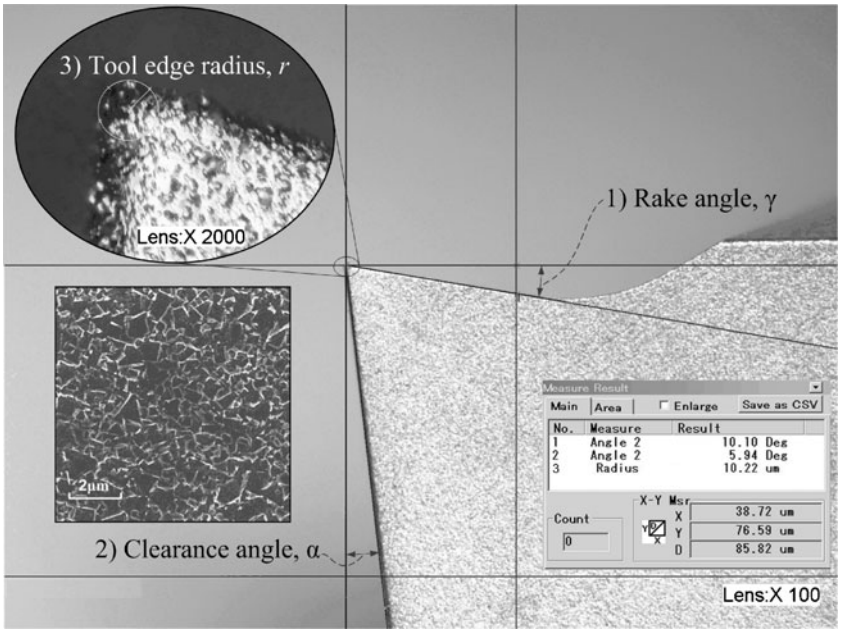

Fig. 6 Tool geometries and microstructures of the WC-Co cutters

thermal softening coefficient, and hardening coefficient. These constants are summarized in Table 1. Moreover, $\varepsilon_{\mathrm{eq}}$,$\underline{\varepsilon}_{eq}$, $\underline{\varepsilon}_0$, T, T_r, and T_m each represents equivalent plastic strain, equivalent plastic strain rate, reference strain rate, working, room and melting temperatures, respectively. The flow stress is thus a function of strain, strain rates, and temperature while homogeneous deformation is assumed.

2.5 Contact behavior

Chip flow motion is reflected from the stick–slide behavior with the modified Coulomb's friction model [25]. Sliding happens when the shear contact stress, τ_{f}, is less than the material shear flow stress, k_{f}, while sticking is realized as τ_{f} exceeds k_{f}. Such frictional phenomenon is represented by Eqs. 20 and 21:

$$\tau_f = k_f \text{ for sticking when } \mu\sigma_n \geq k_f \tag{20}$$

$$\tau_f = \mu\sigma_n \text{ for sliding when } \mu\sigma_n < k_{\mathrm{f}} \tag{21}$$

where σ_n is contact pressure and τ_{f} is shear contact stress at the contact interfaces.

As shown in Fig. 4, the mean friction coefficient, μ_{mean}, was determined as 0.45 under dry condition. Contact

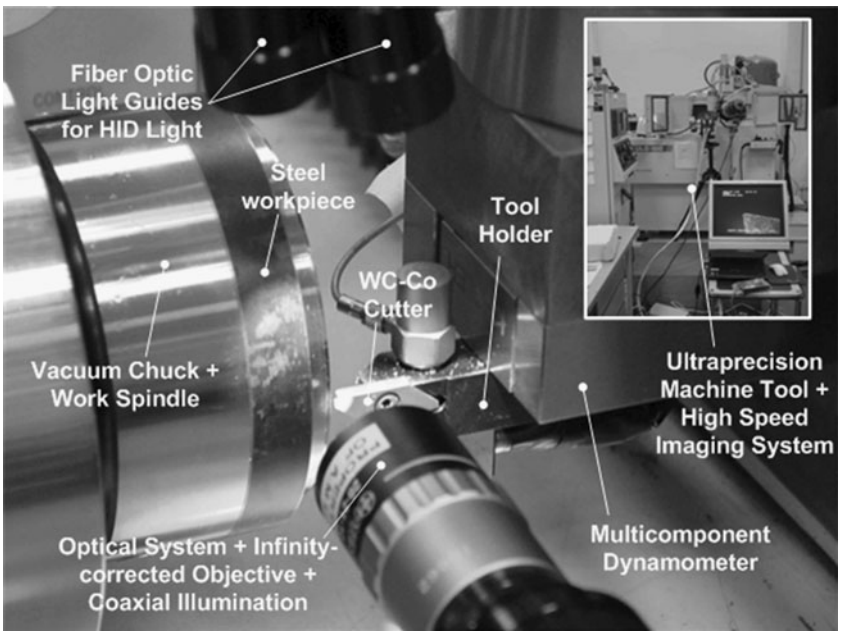

Fig. 7 Illustration of the complete experimental setup for tool-based micromachining of medium carbon steel with cemented tungsten carbide cutters

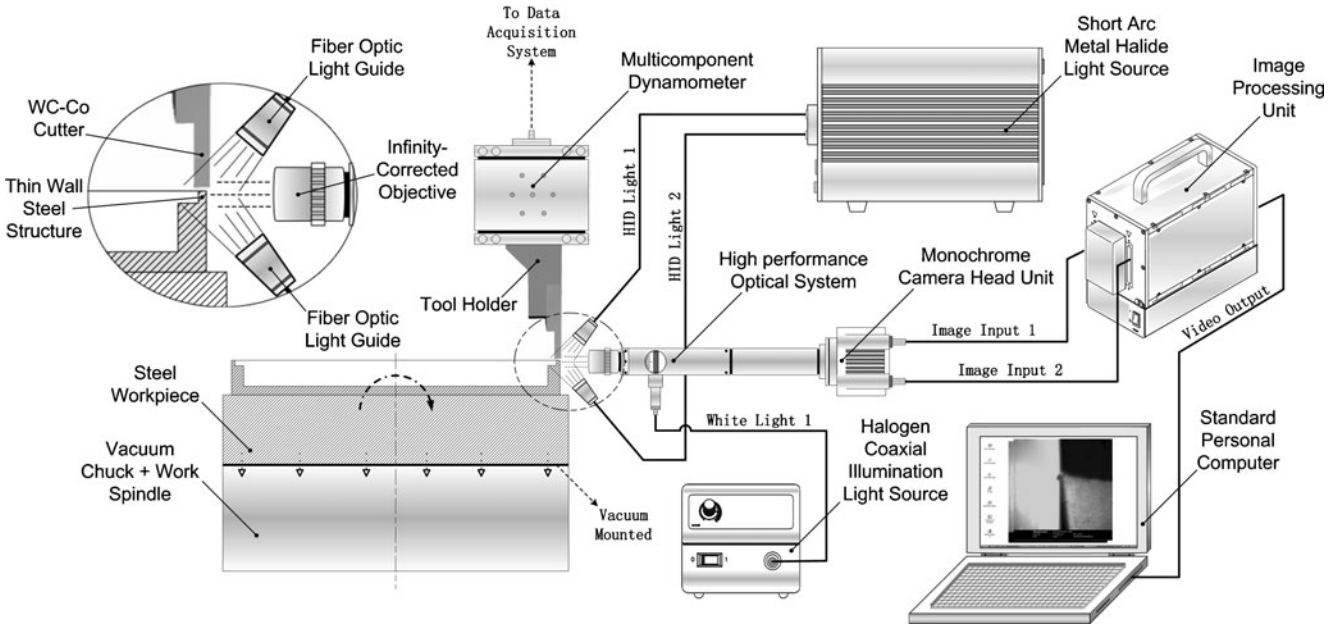

Fig. 8 Schematic diagram of the complete experimental setup which includes the orthogonal machining configuration, the imaging, optical, and lighting systems

fluctuation is recognized as the dynamic cyclical nature of chip formation, and it is acceptable to apply mean values in steady-state conditions [26]. Additionally, previous findings have affirmed the constancy of μ_{mean} and k_{f} during sliding [27] and sticking [28], respectively.

3 Model validations

Experimental validation of the ALE-FE model was performed on an ultra-precision machine tool, Toshiba ULG-100C (H^3), as shown in Fig. 5. It is equipped with aerostatic bearing spindles and the guideways are supported with aerostatic V-V rollers to maintain process stability. Process accuracy is upheld at 1 nm through optical scales with nanometric resolution.

The experimental setup consisted of the orthogonal machining elements, the imaging, optical, and lighting systems. The machining elements included carbide cutters with 0.5-mm straight edges and thin wall steel structures of 0.3-mm thickness created on bulk cylinders. The cutters were P20 carbide (Fig. 6) comprising 0.7-μm WC grains and 10 wt.% Co with a tool edge radius, r, of 10 μm, a tool rake angle, γ, and a clearance angle, α, of 10° and 6°, respectively. The cutter was secured to a hardened steel tool holder and then fixed on a triaxial component dynamometer Kistler 9256C1 MiniDyn, while the steel workpiece was mounted on the vacuum chuck.

A high-speed imaging system Photron Ultima APX was used to capture the process. CMOS sensor of the camera has more than one million pixels to increase light sensitivity so that it could produce full-resolution images under low-light and high-speed condition. To achieve submillimeter field-of-view, an optical system with an image resolution of 300 lp/mm and an infinity-corrected objective lens were coupled with the imaging system. For illumination, a short arc metal halide lighting system with fiber light equipment, Iwasaki MLDS250-2, was used to produce high-intensity light source of minimal flicker. Another coaxial halogen light source was used for fine focusing purposes.

The experimental setup is shown in Fig. 7, and it is schematically illustrated in Fig. 8.

Table 2 Operating conditions for experimental verifications

Cutting speed, V (m/min)	100
Workpiece diameter, D_{w} (mm)	90.0
In-feed rate, f (μm/s)	11.8, 23.6, 35.4…118.0
Undeformed chip thickness, a (μm)	2.0, 4.0, 6.0…20.0
Tool edge radius, r (μm)	10.0
RTS, a/r	0.2, 0.4, 0.6…2.0

4 Experimental verification

The ALE-FE model for micromachining was validated through the main aspects of chip formation mechanics, namely the degree of plastic deformation as determined from the deformed chip thickness, the contact behavior as characterized with the tool–chip contact length, and the overall process mechanics as quantified with the force

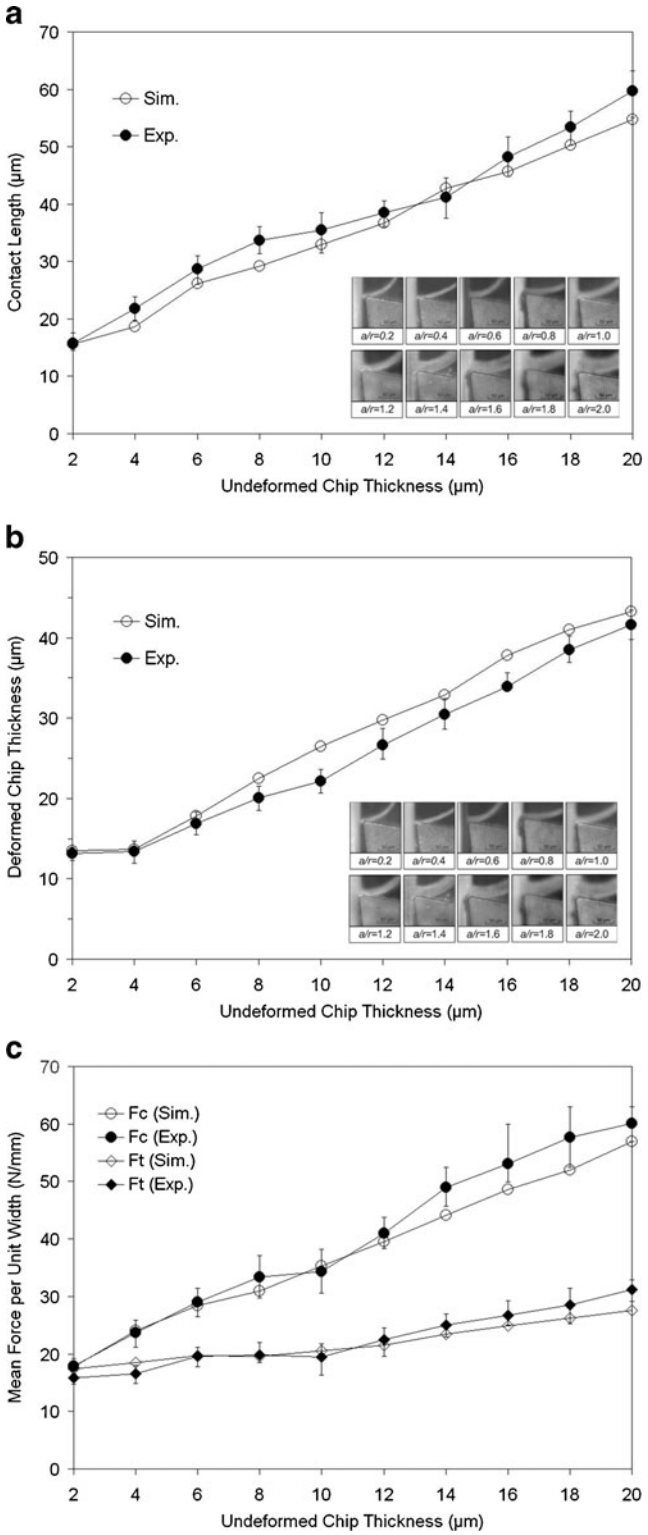

Fig. 9 Comparisons between experimental and simulated results: **a** contact length; **b** deformed chip thickness; and **c** machining forces

components. Experimental verifications under ultra-precision machining criterion were carried out for a wide range of operating conditions as summarized in Table 2. Figure 9a–c illustrates the distributions of simulated and experimental contact length, L_c, deformed chip thickness, t_c, and machining forces, F, respectively.

In general, L_c increased linearly with a where the magnitudes and distribution of simulated and experimental L_c agreed well. The percentages of divergence $\%|\Delta|$ were uniformly maintained at single digit with an average of 8.03%. Similarly t_c had a linear response with a from 4 to 20 μm. The $\%|\Delta|$ remained at single digit at low $a<6$ μm ($a/r<0.6$), while the increase of a widened $\%|\Delta|$ to double digits, 16.46 % being the highest at $a=10$ μm. The average $\%|\Delta|$ was determined as 7.61%.

On the other hand, cutting force, F_c, produced with the ALE-FE model was lower than the experimental findings. Such a trend was similar to the distribution of thrust force F_t. The average $\%|\Delta|$ for F_c and F_t were 5.56% and 6.75%, respectively, where the divergence between experimental and simulated findings increased with a. Both F_c and F_t increased, with a but F_c corresponding greater to a than F_t, and thus, it was observed that the differences between the F_c and F_t became larger with increasing a. In other words, the decrease of machining magnitude promotes the thrust component but reduces the significance of the cutting component. Comparisons between the trends and magnitudes of F_c and F_t as determined experimentally and numerically showed satisfactory agreement.

5 Results and discussions

Sole emphasis on undeformed chip thickness (orthogonal cutting) or feed rate (oblique cutting) is not practical when the tool edge radius effect is significant. Through the decrease of a/r, either by reducing a or increasing r, the effect on the chip formation behavior is amplified.

Figures 10, 11, and 12 illustrate such characteristics in the form of equivalent stress (von Mises) distributions at different cutting speeds, V of 100, 250, and 500 m/min, respectively. For brevity, each case includes three levels of tool rake angle, γ_{tool} of +10°, 0°, and −10°, at a selected range of a/r from above unity (1.8) to below unity (0.4).

5.1 Transitional plastic deformation characteristics

Deformation is imposed by tool edge radius and rake face along the contact length in micromachining. Intense plastic deformation takes place ahead of the edge curvature, which results in material removal from the chip root region.

Under external loading and chip overhang, the deformation zone around the chip root region spreads toward the chip-free boundary, associated with subsurface deformation. It is subjected to concentrated stress confined within a pair of parallel-sided boundaries commonly known as the

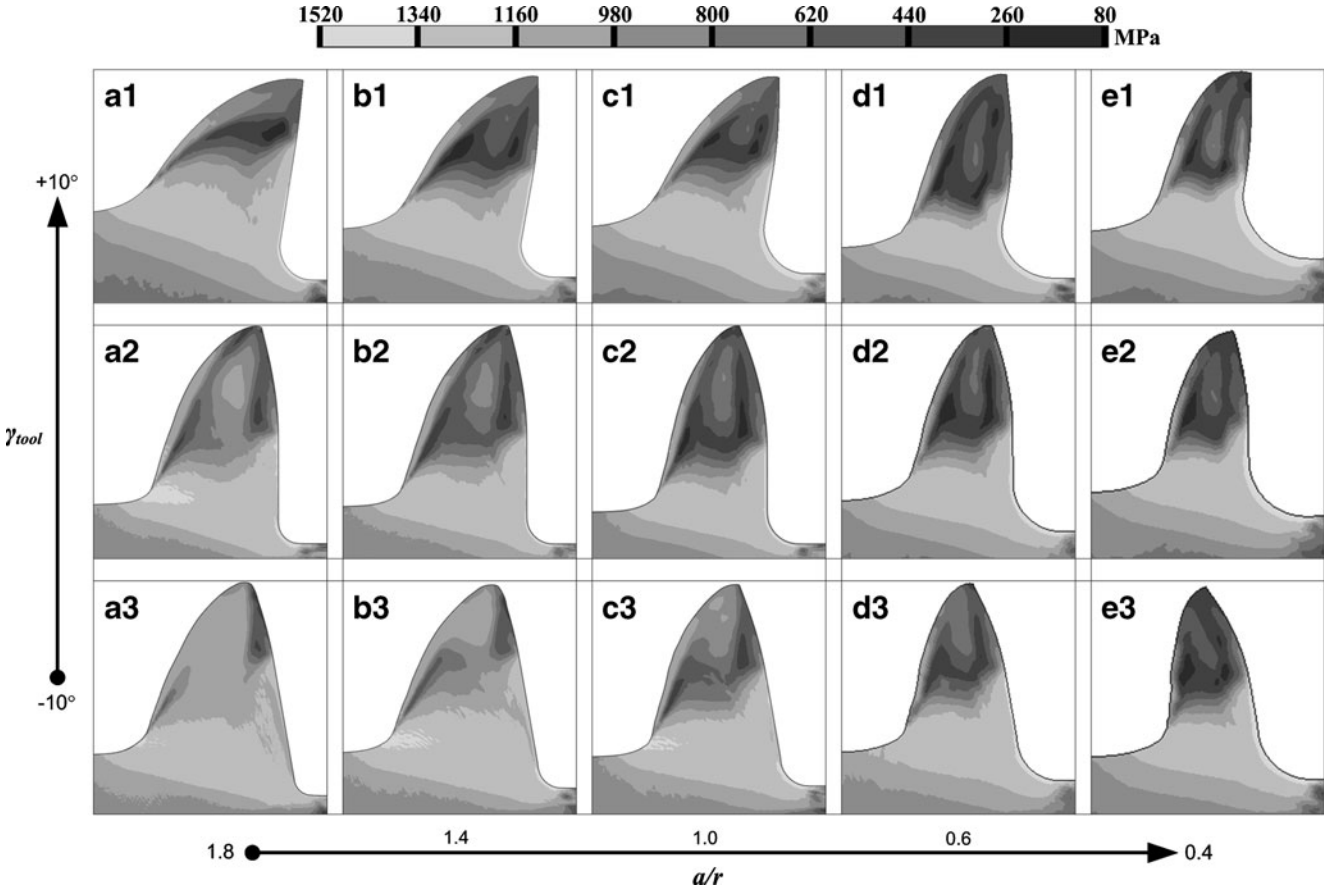

Fig. 10 Transitions in plastic deformation behavior with decreasing a/r using different tool rake angles, γ_{tool}, of +10°, 0°, and −10° at the cutting speed, V, of 100 m/min: $a/r > 1.0$ (*a, b*); $a/r = 1.0$ (*c*); $a/r < 1.0$ (*d, e*)

PDZ. Additionally, another deformation zone is established along the tool rake face which is seen to merge with PDZ at the chip root region known as the SDZ. The presence of SDZ is maintained by constant chip flow during the process. These characteristics are encountered at $a/r > 1.0$ as illustrated by *a1*−*a3* and *b1*−*b3*.

As a/r is decreased to 1.0, materials in the vicinity of the rounded edge curvature undergo a gradual transition of plastic deformation behavior. A relatively larger fraction of PDZ is realized as SDZ shrinks following the reduction of tool–chip contact length on the rake face. This is perceived as an increase of localized plastic flow from that of the cases at $a/r > 1$. Such a chip formation behavior at $a/r=1.0$ is illustrated in *c1–c3*.

Further decrease of a/r below unity leads to an increasingly more aggressive behavioral change. At $a/r< 1.0$, external load is preliminarily imposed by the tool edge radius as the contact length is further reduced, leading to the formations of a small SDZ and therefore a larger fraction of PDZ. Chip growth takes place along the rounded edge curvature instead of fragmentation. After stable contact, interaction is achieved and PDZ appears larger and thicker compared to that of the SDZ, akin to the merger of both deformation zones. These are illustrated by *d1–d3* ($a/r=0.6$) and e*1–e3* ($a/r=0.4$).

The formation of SDZ at a/r from 2.0 to 0.4 takes place because chip flow is extended onto the tool rake face under steady-state machining condition when effective rake angle, γ_{eff}, is formed. The true state of time-invariant stress distributions could only be realized after SDZ is formed provided stable contact lengths are achieved. These cases where $\gamma_{eff}=\gamma_{tool}$ occur extensively at $a/r\geq 0.4$.

5.2 Effective negative rake angle

When effective negative rake angle, $-\gamma_{eff}$, is formed at $a/r= 0.2$, more drastic changes in plastic deformation is encountered. Chip growth ahead of the tool edge radius but the chip could not extend on to the tool rake face even after contact is reached. The magnitude of γ_{eff} changes constantly at first and then becomes stable in a later stage. Figure 13 depicts chip formation under $-\gamma_{eff}$ at $a/r=0.2$ as compared to that at $a/r=0.4$ under $+\gamma_{eff}$.

Under $-\gamma_{eff}$, the equivalent stress becomes highly localized in front of the tool edge radius and results in the sole establishment of PDZ. Stress localization promotes

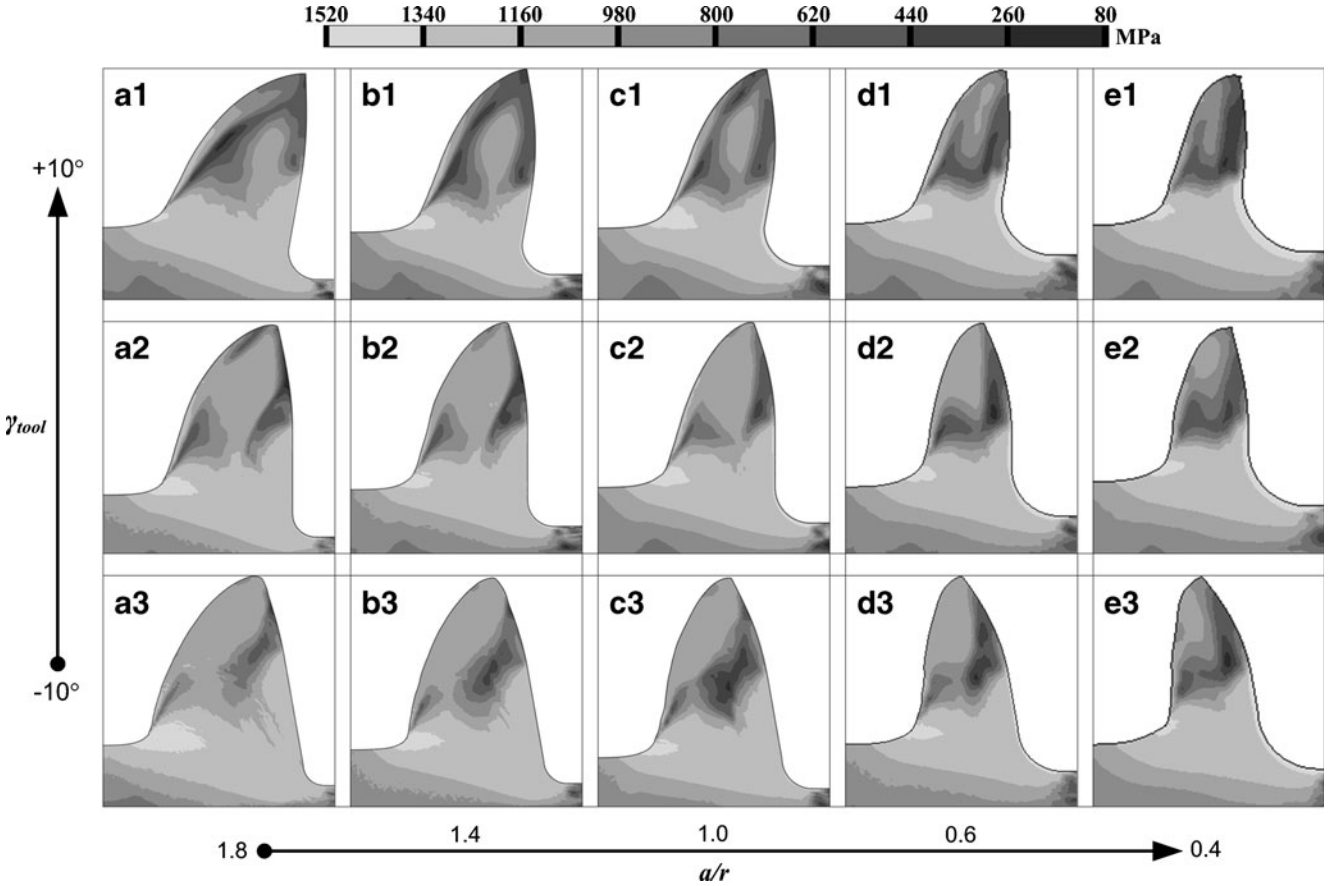

Fig. 11 Transitions in plastic deformation behavior with decreasing a/r using different tool rake angles, γ_{tool}, of +10°, 0°, and −10° at the cutting speed, V, of 250 m/min: $a/r > 1.0$ (*a, b*); $a/r = 1.0$ (*c*); $a/r < 1.0$ (*d, e*)

severe plastic deformation associated with intense compressive stress imposed by the rounded edge curvature. Such deformation transforms chip formation from concentrated shearing at higher a/r to a thrust-oriented mechanism. Such a mechanism transformation is unanimously encountered at a/r=0.2 as illustrated in Fig. 14 under different operating conditions.

These findings clarify the tool edge radius effect on the chip formation mechanism, also the prerequisite for the formation of $-\gamma_{eff}$ at a/r<1.0. Indeed, the purpose of using large nominal positive and negative tool rake angles and a wide range of a/r with constant interval were meant to prove such a conjecture.

5.3 Deformation intensity of the primary deformation zone

The changes in chip formation behavior is driven by the tool edge radius effect on the contact phenomenon where the establishment of SDZ adjacent to the tool rake face is affected by the contact length, while PDZ is expanded by external loading transmitted from the contact interface.

With the dominance of tool edge radius effect at decreasing a/r, the intensity of localized plastic deformation increases correspondingly alongside the formation of effective negative rake angle, $-\gamma_{eff}$. Such progressive elevation of localized deformation on smaller volume of work material leads to a form of intensity increment in plastic deformation across PDZ.

Through the ALE-FE method, characterization of the deformation behavior is attempted through the measurement of PDZ from its (1) width, (2) thickness, and (3) depth as illustrated in Fig. 15. The dimension of each aspect and/or their respective combinations corresponds to the variations in machining condition which governs the mechanics of the micromachining process.

5.3.1 Width of PDZ

The width of primary deformation zone, W_{PDZ}, is measured horizontally from the border of the flow stress region below the cutting tool, across the area that constitutes the chip root, to the opposite border of the flow stress region adjacent to the turning point of the chip-free boundary. Figure 16 illustrates the evolutions of W_{PDZ}.

In general, W_{PDZ} increases with a in a trend of linear proportion. But the linear responses vary for different

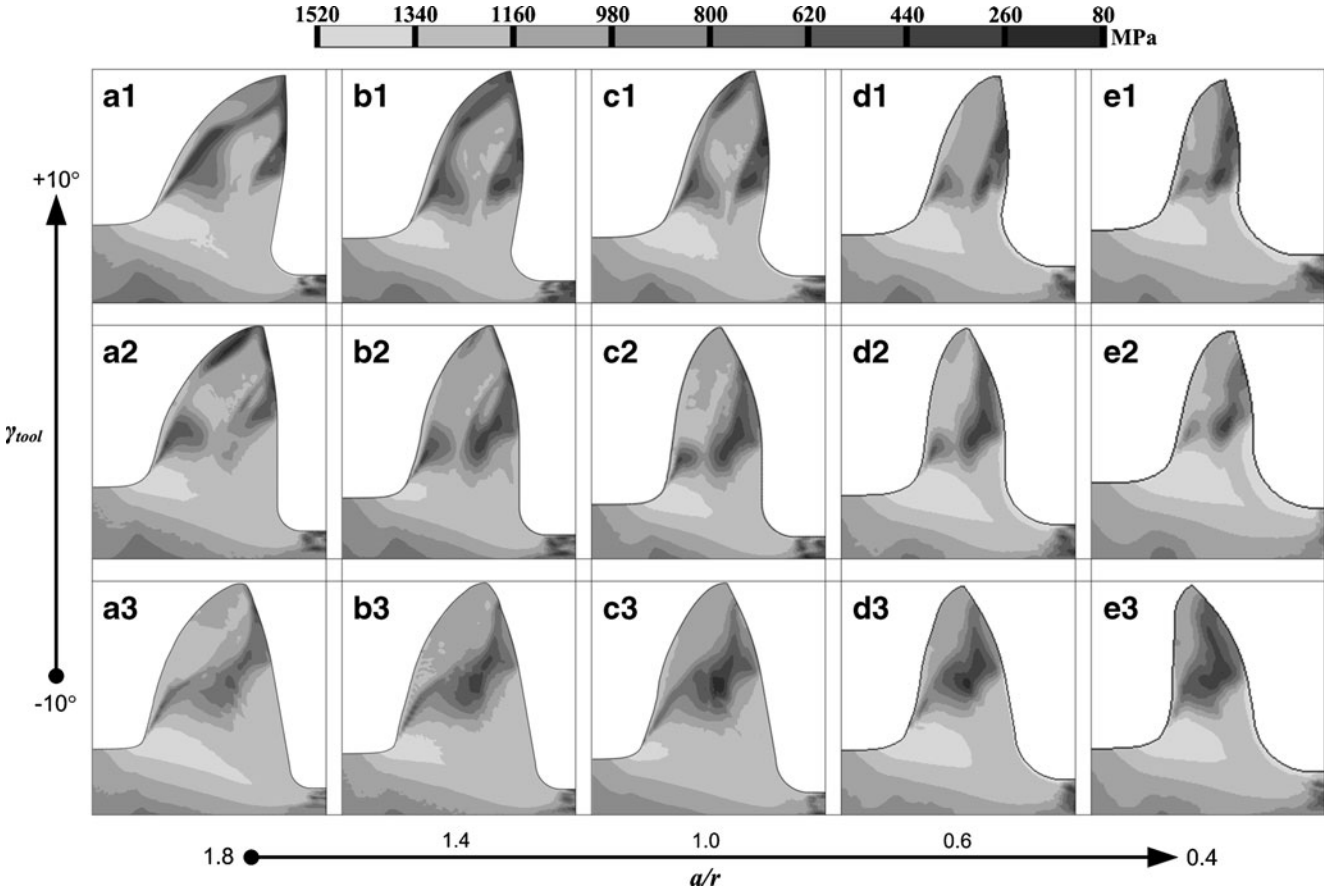

Fig. 12 Transitions in plastic deformation behavior with decreasing a/r using different tool rake angles, γ_{tool} of +10°, 0°, and −10° at the cutting speed, V, of 500 m/min: $a/r > 1.0$ (*a, b*); $a/r = 1.0$ (*c*); $a/r < 1.0$ (*d, e*)

combinations of process parameters as the nature of plastic deformation differs from a particular combination of parameters to the other. The response variable of the linear model is W_{PDZ} and the input variable is a. Each model is associated with its underlying coefficient of determination, R^2, to indicate the goodness of the linear data fittings. Through these linear relationships as summarized in Table 3, the influences of each parameter on W_{PDZ} and/or their combinations would thus be reflected from the slopes and constant interceptions of the straight lines.

At the first approximation, the tool rake angle, γ, has a great effect on the slope magnitudes. Changing γ from

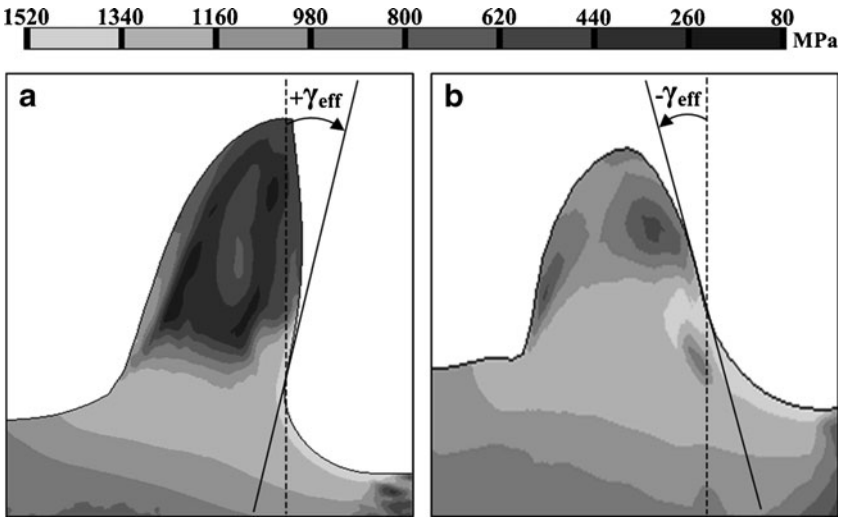

Fig. 13 Contour plots of von Mises stress distributions under different effective rake angles, γ_{eff}. **a** Effective positive rake angle, $+\gamma_{eff}$ at a/r=0.4. **b** Effective negative rake angle, $-\gamma_{eff}$ at a/r = 0.2. A nominal tool rake angle, γ_{tool}, of +10° is used in both **a** and **b**

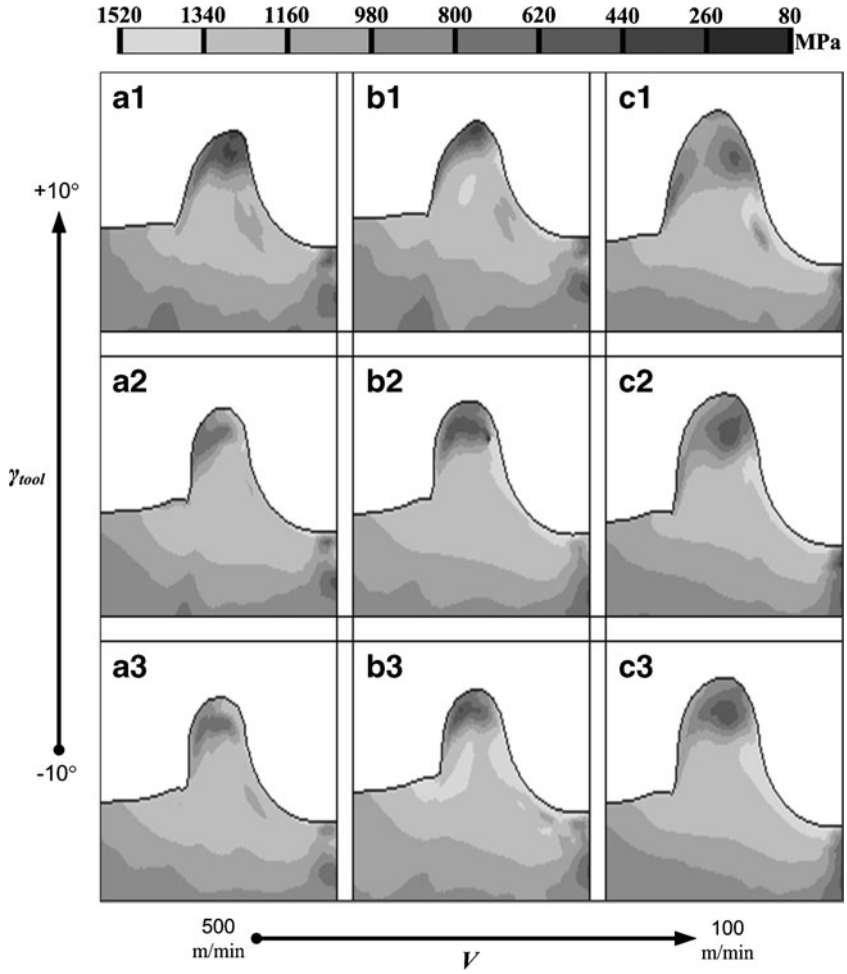

Fig. 14 Highly localized plastic deformation ahead of the tool edge radius under effective negative rake angles, $-\gamma_{eff}$. Such phenomenon is encountered for different combinations of machining conditions at a/r=0.2. *a–c* V of 500, 250, and 100 m/min. *1–3* γ_{tool} of +10°, 0°, and −10°

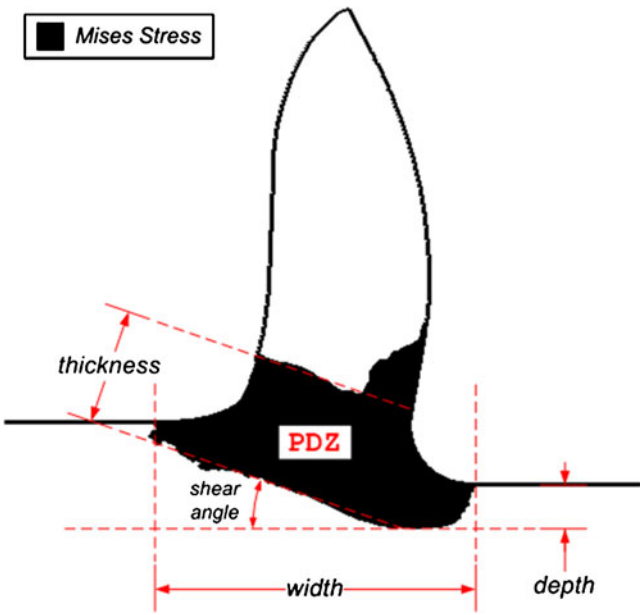

Fig. 15 Characterization of primary deformation zone (*PDZ*) from its width, thickness, and depth

positive to negative, the slope magnitudes vary from approximately 3.0, 4.0, and 5.0 for γ=+10°, 0°, and −10°, respectively. Such findings are unanimously observed for different combinations of r and V. But the effect of cutting speed is less significant as it was determined that the slope magnitudes at different levels of cutting speed have slight variations. On the other hand, the tool edge radius effect has a constant and virtually dominating effect on W_{PDZ} as reflected from the magnitudes of line interception. At various combinations of γ and V, the magnitudes of interception range from 24.0 to 26.0.

5.3.2 Thickness of PDZ

The thickness of primary deformation zone, T_{PDZ}, is measured within a pair of parallel borders from an angle between the horizontal axis that envelop the top and bottom of the flow stress region. The angle between the borders of PDZ and the horizontal axis is regarded as shear angle. Figure 17 illustrates the evolutions of T_{PDZ} at different V. Similar to W_{PDZ}, T_{PDZ} increases linearly with a where the

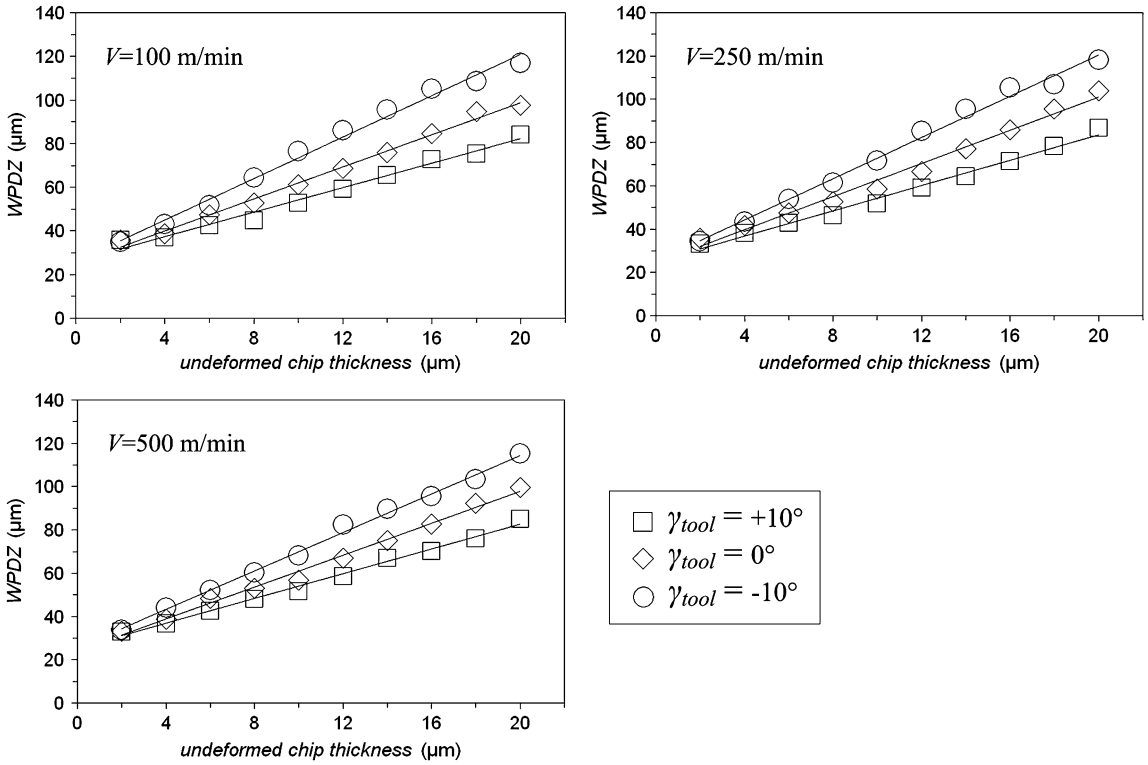

Fig. 16 Linear evolutions of W_{PDZ} with undeformed chip thickness using different tool rake angles and cutting speeds

characteristics of such relationship vary with different process parameters as summarized in Table 4.

Under the influence of tool edge radius, the general trend of T_{PDZ} distribution as reflected from the slope magnitudes is governed by the changes of γ from positive to negative. At V of 100, 250, and 500 m/min, the slope magnitudes vary from 1.09 to 1.87 ($|\Delta|$ = 0.78), 0.97 to 1.73 ($|\Delta|$ = 0.76), and 0.94 to 1.75 ($|\Delta|$ = 0.81), respectively. Such variations due to the changes of γ are virtually constant. On the other hand, the constant and dominating effect of tool edge radius is reencountered in T_{PDZ}. The magnitudes of interception are within the range of 9.0–11.0. The constancy of such an effect on T_{PDZ} is reflected by the constant magnitudes of interception under various combinations of tool rake angle and cutting speed.

5.3.3 Depth of PDZ

The depth of primary deformation zone, D_{PDZ}, is measured from the lowest point of the subsurface flow stress region to the newly generated machined surface. The evolutions of D_{PDZ} at cutting speeds, V, of 100, 250, and 500 m/min are illustrated in Fig. 18.

Unlike the previous cases, the evolutions of D_{PDZ} are more complicated. Although the evolution of D_{PDZ} does exhibit smooth linear trends under some specific combina-

Table 3 Linear relationships between W_{PDZ} and undeformed chip thickness, a

	W_{PDZ}		
	V (m/min)		
γ (deg)	100	250	500
+10°	$W_{PDZ} = 2.80a + 26.21$ $R^2 = 0.9845$	$W_{PDZ} = 2.93a + 25.04$ $R^2 = 0.9881$	$W_{PDZ} = 2.86a + 25.38$ $R^2 = 0.9925$
0	$W_{PDZ} = 3.66a + 25.36$ $R^2 = 0.9936$	$W_{PDZ} = 3.83a + 24.40$ $R^2 = 0.9856$	$W_{PDZ} = 3.69a + 24.01$ $R^2 = 0.9925$
−10	$W_{PDZ} = 4.74a + 26.06$ $R^2 = 0.9902$	$W_{PDZ} = 4.76a + 25.26$ $R^2 = 0.9915$	$W_{PDZ} = 4.44a + 25.55$ $R^2 = 0.9959$

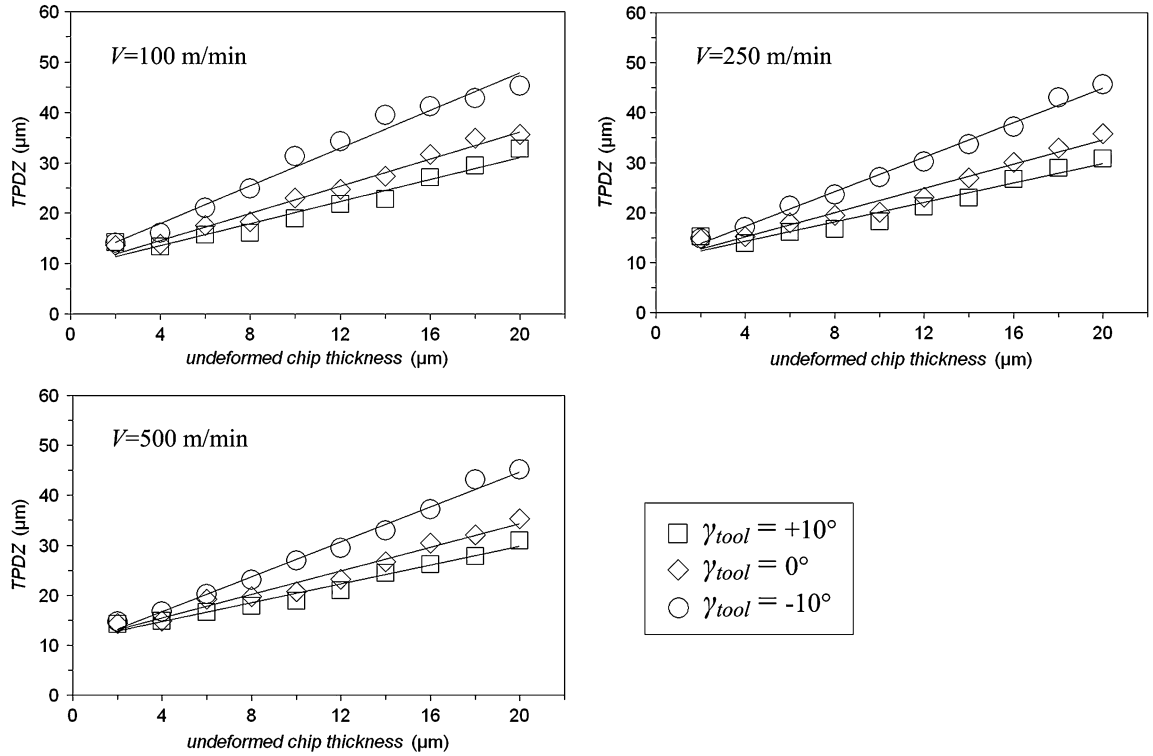

Fig. 17 Linear evolutions of T_{PDZ} with undeformed chip thickness using different tool rake angles and cutting speeds

tions of process parameters, the degree of such linearity is adversely affected by V and γ. The linearity of D_{PDZ} evolutions is sufficiently maintained with reducing undeformed chip thickness, a from 20 to 4 μm (a/r=2.0–0.4). But the magnitudes of D_{PDZ} rebound at a of 2 μm (a/r=0.2) as the localization of plastic deformation increases. This deteriorates the linearity of D_{PDZ} distributions (R^2<0.8) with reducing V of 500 to 100 m/min and increasingly positive rake angles, −10° to +10° as summarized in Table 5.

At lower V of 100 m/min, the evolutions of D_{PDZ} do not exhibit a strong sense of linearity as reflected from the relatively low slope values of 0.05, 0.07, and 0.07 for γ of +10°, 0°, and −10°, respectively. Nevertheless, higher cutting speeds at 250 and 500 m/min improve the linear behavior and elevate the slope values to 0.09, 0.11, and 0.15 and 0.14, 0.18, and 0.22 for γ of +10°, 0°, and −10°, respectively. Besides that, the effect of tool edge radius is also encountered in the case of D_{PDZ}, similar to that of W_{PDZ} and T_{PDZ} with a more consistent influence between 6.0 and 7.0. High cutting speed and negative tool rake play a role in deepening the subsurface deformation.

5.4 Deformed chip thickness: a linear regression analysis

The previous discussion has revolved upon qualitative (Section 5.1) and quantitative (Section 5.3) evaluation of deformation characteristics under the influence of tool edge

Table 4 Linear relationships between T_{PDZ} and undeformed chip thickness, a

	T_{PDZ}		
	V (m/min)		
γ (deg)	100	250	500
+10	T_{PDZ} = 1.09a+9.23 R^2 = 0.9515	T_{PDZ} =0.97a + 10.38 R^2 = 0.9449	T_{PDZ}=0.94a + 10.90 R^2 = 0.9749
0	T_{PDZ} = 1.35a + 9.23 R^2 = 0.9833	T_{PDZ} = 1.21a + 10.29 R^2 = 0.9694	T_{PDZ} = 1.18a + 10.68 R^2 = 0.9734
−10	T_{PDZ} = 1.87a + 10.51 R^2 = 0.9767	T_{PDZ} = 1.73a + 10.35 R^2 = 0.9924	T_{PDZ} = 1.75a + 9.75 R^2 = 0.9959

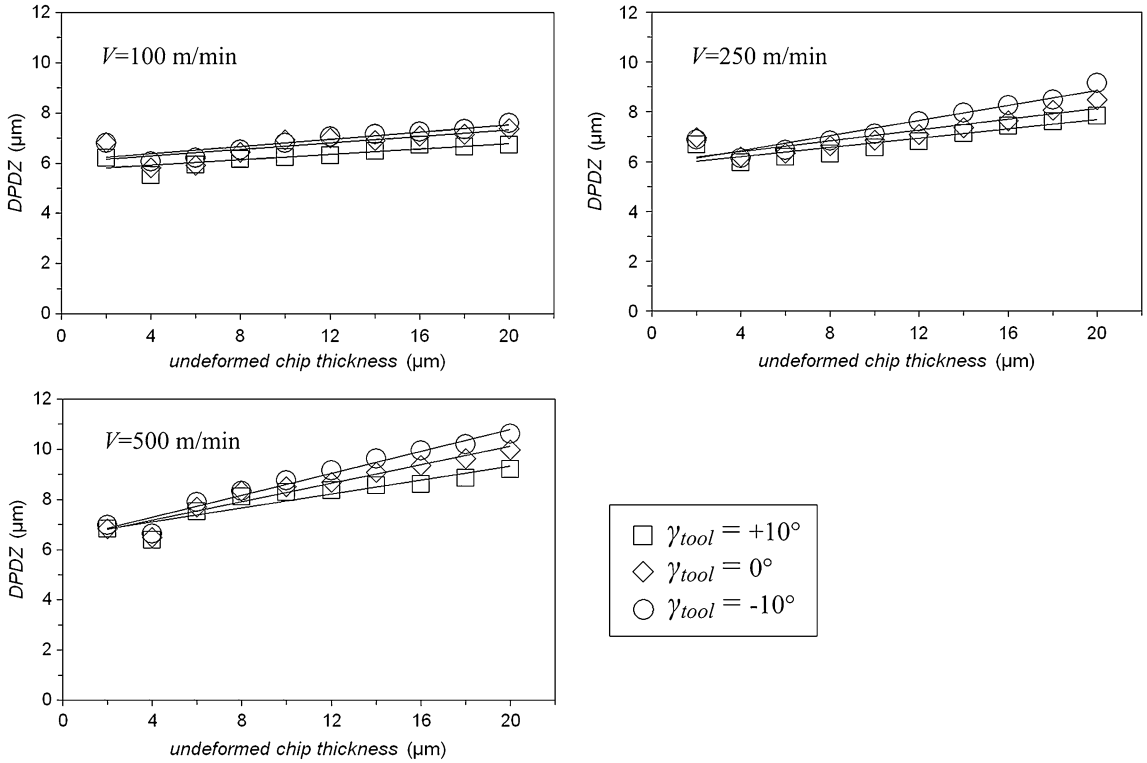

Fig. 18 Linear evolutions of D_{PDZ} with undeformed chip thickness using different tool rake angles and cutting speeds

radius. The present discussion examines such influence on deformed chip thickness, t_c, which indicates the degree of plastic deformation at different operating conditions. In machining, the layer of work material with a predefined undeformed chip thickness, a, undergoes plastic deformation in PDZ which elongates the deformed material-turned-chip to a greater thickness.

Figure 19 depicts the evolutions of t_c for the range of a attempted, and the respective relationships are summarized in Table 6. In general, t_c fits linearly with a as reflected by the magnitudes of coefficient of determination, R^2 beyond 0.98 under various operating conditions. The slope magnitudes range from 1.70 to 4.06. The variations of slope magnitudes increase from 0.08 and 0.44 to 0.45 (average = 0.323) as the cutting speed, V, is decreased from 500 to 250 m/min and then 100 m/min for rake angles, γ = +10°, 0°, and −10°, respectively.

Thus, the linear relationships between t_c and a is primarily governed by tool rake angle followed by cutting speed under the influence of tool edge radius effect.

Table 5 Linear relationships between T_{PDZ} and undeformed chip thickness, a

	D_{PDZ}		
	V (m/min)		
γ (deg)	100	250	500
+10	D_{PDZ}°=0.05a+5.71 R^2 = 0.7322	D_{PDZ}=0.09a+5.83 R^2 = 0.8017	D_{PDZ}=0.14a+6.55 R^2 = 0.8672
0	D_{PDZ} = 0.07a+6.02 R^2 = 0.5709	D_{PDZ}=0.11a+5.97 R^2 = 0.7961	D_{PDZ}=0.18a+6.43 R^2 = 0.9345
−10	D_{PDZ}=0.07a+6.10 R^2 = 0.9767	D_{PDZ}=0.15a+5.83 R^2 = 0.8913	D_{PDZ}=0.22a+6.41 R^2 = 0.9959

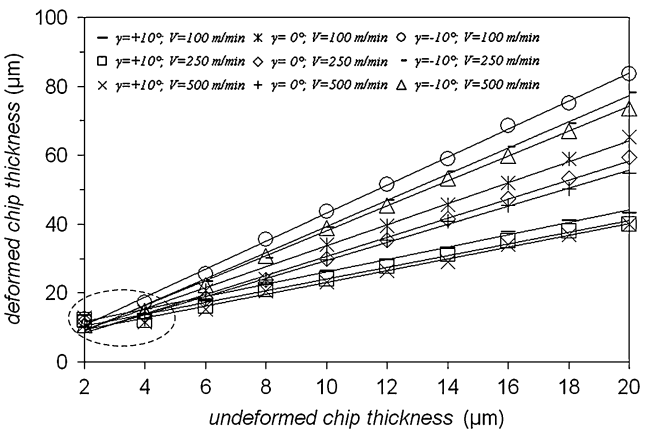

Fig. 19 Linear evolutions of deformed chip thickness with undeformed chip thickness

Combinations of negative rake angle and low cutting speed yield the highest slope magnitudes and thus the steepest straight line. The reversal of both parameters to positive rake angle and increasing cutting speeds produce a lower range of slope magnitudes and therefore straight lines with lesser steepness. These are reflected from the variations of slope magnitudes increase from 1.90 to 2.09 and then 2.27 (average = 2.087) at V=500, 250, and 100 m/min, respectively, as γ is reduced from +10° to 0° and then −10°. Thus, the significant influences of negative rake angle on the magnitudes of t_c at low cutting speed and vice versa are clearly expressed.

Nevertheless, slight t_c rebounds at a of 2 μm (a/r=0.2) perceived as a diversion from the regular linear distribution which has been uniformly encountered under all conditions. Such a finding is largely due to severe localized plastic deformation following the transition of chip formation behavior.

Indeed, the effect of tool edge radius on this aspect could be further evaluated through the distributions of normalized deformed chip thickness, t_c/a with a/r as presented in Fig. 20. With the increase of a/r from 1.0 to 2.0, the t_c/a distributions show a general saturating trend toward the extreme end but at varying magnitudes of saturation for different operating conditions. But for $a/r < 1.0$, elevations in t_c/a are generally observed, but more rapid increasing rates are encountered with γ of 0° and +10°.

These findings are attributed to the amplification of tool edge radius effect on plastic deformation with the decrease of a/r below unity. Indeed, the "bounce back" phenomenon in t_c/a for γ of −10° within $0.6<a/r<1.0$ is also governed by this factor. Such a phenomenon is exclusive for a γ of −10° as chip formation is subjected to the complementary influences of both tool edge radius and tool rake angle within that particular range of a/r. This also explains the drop of t_c/a when a/r is further reduced below 0.6 when the influence of negative tool rake angle becomes weaker. Eventually, as a/r is reduced down to 0.2, chip formation is performed entirely by the rounded edge curvature which leads to intense localized deformation. Such plastic deformation is effectively reflected from the respective high t_c/a magnitudes at a/r=0.2.

Table 6 Linear relationships between deformed chip thickness, t_c, and undeformed chip thickness, a, at different cutting speeds and tool rake angles

	r =10μm V (m/min)		
γ (deg)	100	250	500
+10	$t_c = 1.79a+8.09$	$t_c = 1.70a+7.04$	$t_c = 1.71a+5.96$
	$R^2 = 0.9914$	$R^2 = 0.9896$	$R^2 = 0.9939$
0	$t_c = 3.05a+3.21$	$t_c = 2.76a+3.09$	$t_c = 2.61a+3.39$
	$R^2 = 0.9908$	$R^2 = 0.9931$	$R^2 = 0.9970$
−10	$t_c = 4.06a + 2.56$	$t_c = 3.79a + 1.46$	$t_c = 3.61a + 1.94$
	$R^2 = 0.9982$	$R^2 = 0.9970$	$R^2 = 0.9982$

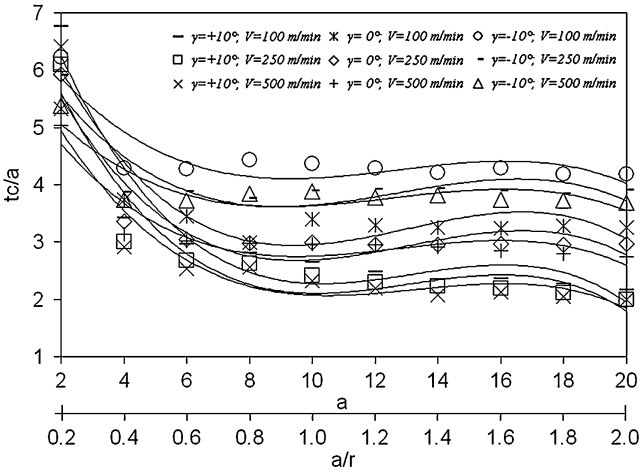

Fig. 20 Evolutions of normalized undeformed chip thickness, t_c/a, to the ratio of undeformed chip thickness to tool edge radius, a/r, at different tool rake angles, γ, and cutting speeds, V

6 Conclusions

Based on the findings in this study, the following are concluded:

- The decrease of a/r reduces tool–chip contact length and elevates the degree of localized deformation which brings about the shrinkage of secondary deformation zone and a larger fraction of primary deformation zone.
- The changes in chip formation behavior is transitional with varying a/r as reflected by the dimensions of primary deformation zone from its width (W_{PDZ}), thickness (T_{PDZ}), and depth (D_{PDZ}).
- Chip formation transforms from concentrated shearing to a thrust-oriented mechanism below the a/r threshold, under effective negative rake angle where the formation of secondary deformation zone is suppressed.
- Thrust-oriented chip formation mechanism involves high-intensity plastic deformation as indicated by the large magnitudes of deformed chip thicknesses, t_c.

Acknowledgments The authors would like to express their appreciation to the university staff of Supercomputing & Visualization Unit, Advanced Manufacturing Laboratory, and Impact Mechanics Laboratory of National University of Singapore for their valuable technical support. Financial support by the Singapore Institute of Manufacturing Technology (SIMTech) under the CRP (no. U04-M-136B) is also gratefully acknowledged.

References

1. Masuko M (1956) Fundamental research on metal cutting. B JSME 22:371–377
2. Albrecht P (1960) New developments in the theory of the metal-cutting process. J Eng Ind–T ASME Nov, pp 348–358
3. Finnie I (1963) A comparison of stress strain behavior in cutting with that in other materials tests. Int Res Prod Eng, pp 76–82
4. Bitans K, Brown RH (1965) An investigation of the deformation in orthogonal cutting. Int J Mach Tool Des Res 5:155–165
5. Nakayama K, Tamura K (1968) Size effect in metal-cutting force. J Eng Ind–T ASME Feb, pp 119–126
6. Abdelmoneim ME, Scrutton RF (1974) Tool edge roundness and stable build-up formation in finish machining. J Eng Ind–T ASME Nov, pp 1258–1266
7. Basuray PK, Misra BK, Lal GK (1977) Transition from ploughing to cutting during machining with blunt tools. Wear 43:341–349
8. Komanduri R, Chandrasekaran N, Raff LM (1998) Effect of tool geometry in nanometric cutting: a molecular dynamics simulation approach. Wear 219:84–97
9. Moriwaki T, Okuda K (1989) Machinability of copper in ultra-precision micro diamond cutting. Annals CIRP 38:115–118
10. Ikawa N (1991) Ultraprecision metal cutting—the past, the present and the future. Annals CIRP 40:587–594
11. Lucca DA, Rhorer RL, Komanduri R (1991) Energy dissipation in the ultraprecision machining of copper. Annals CIRP 40:69–72
12. Moriwaki T, Sugimura N, Luan S (1993) Combined stress, material flow and heat analysis of orthogonal micromachining of copper. Annals CIRP 42:75–78
13. Lucca DA, Seo YW, Rhorer RL (1994) Energy dissipation and tool–workpiece contact in ultra-precision machining. STLE Tribol T 37:651–655
14. Inamura T, Takezawa T, Kumaki Y (1993) Mechanics and energy dissipation in nanoscale cutting. Annals CIRP 42:79–82
15. Inamura T, Takezawa T, Kumaki Y, Sata T (1994) On a possible mechanism of shear deformation in nanoscale cutting. Annals CIRP 43:47–50
16. Fang FZ, Zhang GX (2003) An experimental study of edge radius effect on cutting single crystal silicon. Int J Adv Manuf Technol 22:703–707
17. Liu K, Li XP, Rahman M, Neo KS, Liu XD (2007) A study of the effect of tool cutting edge radius on ductile cutting of silicon wafers. Int J Adv Manuf Technol 32:631–637
18. Arefin S, Li XP, Rahman M, Liu K (2007) The upper bound of tool edge radius for nanoscale ductile mode cutting of silicon wafer. Int J Adv Manuf Technol 31:655–662
19. Li XP, Cai M, Rahman M, Liang S (2009) Study of the upper bound of tool edge radius in nanoscale ductile mode cutting of silicon wafer. Int J Adv Manuf Technol. (in press). doi:10.1007/s00170-009-2347-6
20. Kim J-D, Kim DS (1995) Theoretical analysis of micro-cutting characteristics in ultra-precision machining. J Mater Process Tech 49:387–398
21. Ozel T, Zeren E (2005) Finite element method simulation of machining of AISI 1045 steel with a round edge cutting tool. Proceedings of the 8th CIRP International Workshop on Modelling of Machining Operations, Chemnitz, Germany, pp 533–542
22. Stein E, Borst R, Hughes TJR (2004) Encyclopedia of computational mechanics, vol 1: fundamentals. Wiley, New York
23. Zhao G-J (1987) A method based on the polar decomposition theorem to analyze and compute the strain and rotation. Proceedings of the 20th Midwestern Mechanics Conference, West Lafayette, IN, Purdue University, pp 499–503
24. Johnson GR, Cook WH (1983) Constitutive model and data for metals subjected to large strains, high strain rates and high temperatures. Proceedings of the 7th International Symposium on Ballistics, pp 541–547
25. Zorev NN (1963) Interrelationship between shear process occurring along the tool face and on the shear plane in metal cutting. Int Res Prod Eng, pp 42–49
26. Machado AR, Wallbank J (1997) The effect of extremely low lubricant volumes in machining. Wear 210:76–82
27. Iwata K, Osakada K, Terasaka Y (1984) Process modeling of orthogonal cutting by the rigid-plastic finite element method. J Eng Mater–T ASME 106:132–138
28. Shirakashi T, Usui E (1974) Simulation analysis of orthogonal metal cutting mechanism. Proceedings of the International Conference of Production Engineering, Tokyo, pp 535–540